Energy materials

The novel behavior of photoelectrochemical property of annealing TiO$_2$ nanorod arrays

Shangrong Chen[1] , Changlin Li[1] , and Zhongyu Hou[1,*]

[1] National Key Laboratory of Science and Technology on Micro/Nano Fabrication, Department of Micro/Nano Electronics, School of Electronic Information and Electrical Engineering, Shanghai Jiao Tong University, Shanghai 200240, People's Republic of China

ABSTRACT

Photoelectrochemical (PEC) properties of as-prepared TiO$_2$ nanorod arrays (NRAs) are shown to be positively related to the annealing temperature in the studies. We report the experimental evidences on the saturation behavior of PEC properties responding to the annealing temperature of the TiO$_2$ NRAs. The effect of the annealing temperature ranging in 250–550 °C on the surface morphology, crystalline size, crystal structure, surface chemical states, band-gap, optical and photoelectrochemical performance has been scrutinized. It is found that the photocurrent density of the annealing TiO$_2$ NRAs at 450 °C under air atmosphere for 1 h is the highest and about six times higher than that of the as-prepared samples. However, the PEC performance has been deteriorated with further increase in temperature. The underlying mechanism could be understood by the morphology and crystal size variations of the TiO$_2$ NRAs annealed. It is evidently shown that the PEC performances exhibit strong optimization behavior in response to the annealing temperature, which is an effective method for further improving PEC property for water splitting and other electrical device performance of the TiO$_2$-based materials.

Introduction

Since 1972, TiO$_2$, applied as a photoanode in the photoelectrochemical (PEC) water splitting to produce hydrogen, was first reported by Fujishima and Honda [1]; it is a promising semiconductor material for PEC water splitting to produce clean energy. However, PEC performance of the as-prepared TiO$_2$ is poor and can be greatly improved for the heat treatment samples or sensitized by other materials.

Due to its many merits, such as nontoxicity, anticorrosion and excellent photoelectric property, TiO$_2$-based functional semiconductor material has been widely applied in many electronic devices, such as PEC water splitting to produce hydrogen [2–8], quantum dot or dye-sensitized solar cells (DSSC) [9–13], photovoltaic devices and photocatalysis degrading polluted water and so on [14, 15]. However, TiO$_2$ is a wide band-gap semiconductor material (3.0–3.2 eV) [16] so there is a still challenge to utilize TiO$_2$ for all kinds of photovoltaic devices.

Address correspondence to E-mail: zhyhou@sjtu.edu.cn

TiO_2 has been extensively researched as independent photocatalyst or substrate by the numerous researchers for enhancing the photoelectric property of TiO_2 and enlarging its absorbing edge of the visible light. There are three ways to improve the performance of TiO_2: first, photoelectric property of TiO_2 can be improved by changing surface morphology, such as nanorod [3], nanosheet [17], nanotube [18] and so on. Second, the doping can tune the band-gap of TiO_2 semiconductor, e.g., carbon [19, 20], nitrogen [21–25], iodine [26], sulfur [27], metal elements tin [28] and co-doping such as tungsten and carbon to enhance the TiO_2 PEC activity [29]. Third, the decoration or sensitization TiO_2 with the other semiconductors or metal has been applied to improve the PEC activity, such as carbon quantum dot (QD) [30, 31], Pd QD [32], ZnO [33, 34], CdS [35–37], CdSe [38, 39] and MoS_2 [40] and so on. Although the photoelectric performance can be improved by the surface image, doping and decorating or sensitizing, the heat treatment will also greatly affect the PEC activity.

The synthesis methodology and post-treatment are very crucial for synthesizing TiO_2 for PEC water splitting. Among the three crystalline patterns of TiO_2, the rutile phase synthesized by hydrothermal method is the most stable phase and the investigation of mechanism about heat treatment and PEC performance has been reported in some studies. For example, Fàbrega et al. [41] investigated the annealing TiO_2 nanorod photoanodes for water splitting by transmission line theory; Gu et al. [42, 43] reported the improved PEC performance of TiO_2 nanorod arrays by post-treatment and influence of annealing ambient for TiO_2 nanorod arrays (NARs) on the photoelectric and PEC properties. However, there are few studies about the optimization behavior in the annealing treatment effect on the TiO_2 photoelectric activity and the mechanism is also not well understood.

In the present paper, the enhanced PEC property behavior of the rutile TiO_2 in a wide range of annealing temperatures has been scrutinized. The as-prepared (or pristine) and annealing TiO_2 NRAs have been carefully compared, including the surface morphology, grain size, crystallinity, band-gap, surface chemical states, optical and PEC properties. It is found that there is an optimum point of the annealing temperature, corresponding to the comparatively best PEC activities. The results in this work may be used to improve the PEC-based water splitting, through mechanisms other than those underlying the heterostructure-based methodologies.

Experiment

Preparation of photoanodes

Preparation of TiO_2 NRAs

All chemical reagents are of the analytic grade and used as-received without further purification in the experiment. Vertically aligned TiO_2 NRAs were grown on transparent conductive fluorine-doped tin oxide (FTO and 7 Ω/square) substrates by one-step hydrothermal synthesis in previous reports [12, 39, 44]. In the experiment process, the FTO substrates first were ultrasonically cleaned with acetone, ethanol and deionized water for 10 min, respectively, and followed by drying in flow of N_2. In short, 30 mL deionized water and 30 mL concentrated hydrochloric acid (mass fraction 36–38%) were mixed in a beaker by stirring under air condition for 10 min. Then, 1 ml titanium butoxide (TBOT $\geq$ 99.0%) was added to the mixture dropwise and stirred for another 10 min. After two pieces of FTO substrate were symmetrically placed at an angle against the wall of the Teflon liner with the conductive side facing down, the solution was transferred into a Teflon-lined stainless-steel autoclave of 100 mL volume. The hydrothermal synthesis was carried out at 150 °C for 12 h in a drying oven. After synthesis, the autoclave was cooled down to room temperature in air, and the FTO substrates were taken out to rinse with deionized water for $\sim$ 1 min and dried by N_2.

Post-treatment of TiO_2 NRAs

The samples have been classified into five groups, i.e., the pristine, the annealing at 250 °C, 350 °C, 450 °C and 550 °C, respectively. The annealing time of the samples at each temperature is all 1 h. The maximum annealing temperature has been limited to 550 °C, because the glass transition temperature is about 650 °C and the glass substrate may be damaged when the annealing temperature is above 550 °C. In order to compare the microstructure changes of the samples induced during annealing process using transmission electron microscope

(TEM), for every samples annealed at 450 °C, we have scraped off some area of samples to perform the TEM characterization before and after the annealing treatments. This operation may increase the reliability of the data, comparing to direct using different samples, because the uniformity of the nanorods in the very same sample should be better. For the preparations of TiO_2 nanorod array photoanodes, 1 cm^2 area was exposed and the other parts of the sample surface were sealed by the white opaque silica gel.

Characterizations

The surface conditions of the pristine and annealing TiO_2 NRAs at different temperatures were characterized by Raman imaging combined with field emission scanning electron microscope (SEM, TESCAN-MAIA WITEC MAIA3 GMU model 2016, Czech) operating at 5 kV. TEM (TALOS F200X, USA) and high-resolution TEM (HR-TEM) operating at 200 kV were used to analyze the microstructures of the samples. The crystalline structure of all the TiO_2 NRAs was characterized by X-ray diffraction (XRD, D8 ADVANCE, Germany) with diffraction angles, ranging in 20–80°, using Cu Kα radiation (λ = 0.15406 nm) source at a voltage of 40 kV and a current of 40 mA. The UV–Vis absorption spectrum was carried out using a UV–Vis spectrophotometer (Lambda 950, PerkinElmer, USA). Photoluminescence (PL) emission spectrum of the samples was recorded on a PerkinElmer LS-55 type fluorescence spectrophotometer, and the light wavelength excited is 325 nm at room temperature.

Photoelectrochemical measurements

All the PEC measurements were taken in a square quartz glass cell using a conventional three-electrode configuration. The electrolyte was 0.5 M Na_2SO_3 (pH = 9.85) aqueous solution [45]. All of the samples were acted as working electrode where illumination area was 1 cm^2. The Pt plate and Ag/AgCl (saturated KCl) were acted as the counter electrode and the reference electrode, respectively. The reversible hydrogen electrode (RHE) potential is converted by the Ag/AgCl using the following relationship [35, 46]:

$$E_{RHE} = E_{Ag/AgCl} + 0.059PH + E^0_{Ag/AgCl}, \tag{1}$$

where $E_{Ag/AgCl}$ is the experimentally measured potential and $E^0_{Ag/AgCl}$ = 0.1976 V at 25 °C for an Ag/AgCl reference electrode in saturated KCl aqueous solution. Before the experiment, the electrolyte was degassed with nitrogen in order to remove dissolved oxygen. All measurements were taken under simulated sunlight 100 mW cm^{-2} with 500 W Xenon lamp in a sunlight simulator equipped with an AM 1.5G global filter as light source (AuLight, Beijing, CEL-S500). The intensity of the incident light was controlled at 100 mW cm^{-2} to use a silicon digital power meter (PM100D, THORLABS) by changing the distance between the digital power meter and light source. The photocurrent measurement was taken at scale rate of 50 mVs^{-1} on an electrochemical station (CHI660E, CH Instrument Inc. Shanghai) by linear sweep voltammetry (LSV, J–V curves).Transient photocurrent I–t curves were acquired under chopped light irradiation with on/off intervals of 20 s (0.025 Hz) at an applied potential of 0 V versus Ag/AgCl. In order to investigate the effect of the different electrolyte, 0.5 M Na_2SO_3 and Na_2SO_4 aqueous solution were acted as electrolyte in the experiment.

Results and discussion

Surface morphology

The SEM morphologies of the different samples are shown in Fig. 1. The pristine TiO_2 is responding to Fig. 1a, b, and the annealing temperature of Fig. 1c–h is 350, 450 and 550 °C for 1 h, respectively. The morphology of sample annealed at 250 °C is not shown because of its significant similarities to those of the pristine. Three aspects are described for the character of the samples. First, it is shown that the TiO_2 NRAs are uniformly, densely and vertically distributed on the entire surface of the FTO substrate and the TiO_2 nanorod is almost square in top view. Besides, the side walls of the TiO_2 nanorods are smooth. It should be emphasized that this is the common condition across all the pristine samples. Second, there are many apexes on the top of the TiO_2 as shown in Fig. 1b. However, the apexes are gradually disappeared with the annealing temperature increase. The top of the TiO_2 nanorods becomes gradually smooth, but it is noted that the previous apexes have also become smooth in Fig. 1h. The

Figure 1 The SEM morphologies of the pristine and annealing TiO$_2$ samples: **a** and **b** pristine, **c** and **d** 350 °C, **e** and **f** 450 °C, **g** and **h** 550 °C.
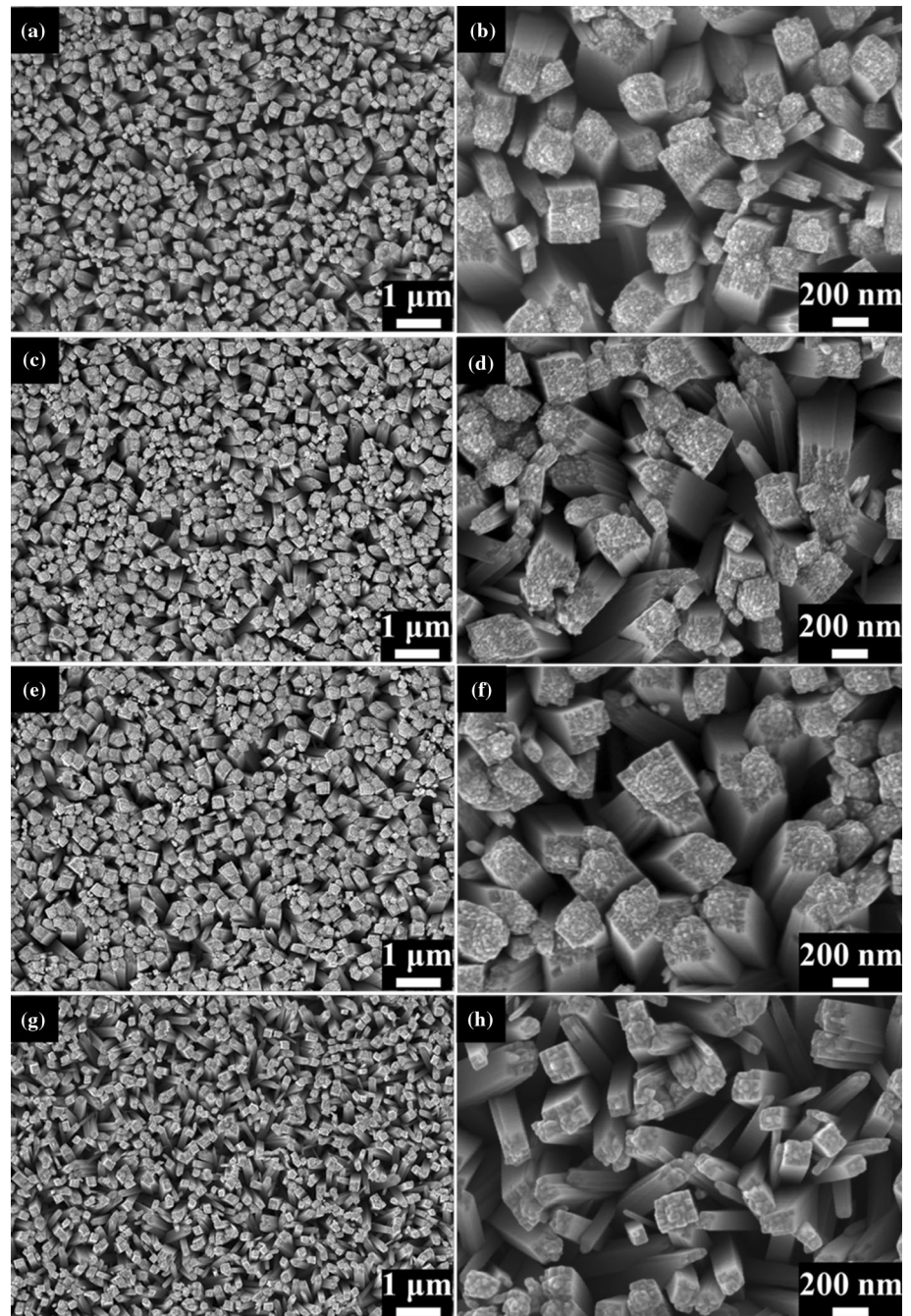
phenomena might be interpreted that TiO$_2$ nanorods would become more compact or shrunken as the annealing temperature increases [47]. Third, it can be found that the average diameter of the square columns after annealing is less than that before the annealing treatment. The average length of nanorods is $\sim$ 2.0 μm by the measuring. This can be explained by that the pristine nanorods are composed of smaller columns so that they are reconstructed after high-temperature annealing. As a result, the gaps between the nanorods become larger as the annealing temperature increases [47].

X-ray diffraction characterization

Figure 2 displays the XRD diffraction patterns of the samples and the FTO substrate. All the diffraction peaks recorded for the FTO substrate are identified (JPCDS card no. 41-1445) as purple line and labeled with symbol ◆ in Fig. 2. Hydrothermal-grown TiO$_2$

NRAs have a rutile structure (JPCDS no. 21-1276; space group: p42/mnm (136); $a = b = 0.4593$ nm, $c = 0.2595$ nm), which is consistent with the other papers [44, 48]. The characteristic diffraction peaks except for those of the FTO substrate appear at 36.08°, 41.22°, 62.74°, 69.00° and 69.79°, which are corresponding to (101), (111), (002), (301) and (112) crystalline plane of TiO_2. It is found that the two diffraction peaks of TiO_2 at 54.32° and 65.48° overlap with the peaks of FTO substrate (not marked in Fig. 2). It is found that the XRD patterns are identical before and after the annealing treatment, regarding the spectrum positions. This indicates that no other phases appear during the annealing processes. However, the peak intensity of TiO_2 annealed at 450 °C is strengthened at 62.74°, indicating that the crystallinity and orientation direction of TiO_2 change noticeably, which will affect the PEC performance. It is found that the pristine and annealing TiO_2 nanorods are made up of monocrystalline columns, even after the annealing treatment, no obvious structure or lattice distortion can be observed, which is in agreement with Refs. [41, 42].

Surface chemical state

In order to investigate the detailed surface chemical states of all the samples, X-ray photoelectron spectroscopy (XPS) spectra are shown in Fig. 3. The data have been calibrated with the carbon peaks at 284.8 eV. As shown in Fig. 3a, it is found that the two characteristic peak positions of the Ti $2p_{3/2}$ and Ti

$2p_{1/2}$ located at ca. 458.8 and ca. 464.5 eV, respectively, with 5.7 eV for the spin–orbit splitting energy, which are consistent with other references [44, 49, 50]. However, it is discovered that the peak values of the annealing samples show slightly but non-negligible negative shifting. This phenomenon can be explained by the fact that the transformation of Ti^{4+} to lower valence titanium cation will increase the oxygen vacancies of TiO_2 NRAs during the heat treatment [51]. It is in accordance with the theory expectations that the binding energy is negatively related to the electron cloud density and the lower binding energy corresponds to the higher electron density [50, 52].

In Fig. 3b, it is found that there are the two peaks for the O 1s XPS core level spectra of all the samples. One peak position locates at ca. 530.1 eV, which is the characteristic value of Ti–O bonds in TiO_2 NRAs, and another peak position is at ca. 531.7 eV, which can be attributed to hydroxyl groups (O–H) in the TiO_2 NRAs [33]. Notably, the general trend of both the Ti 2p and O 1s positions shifts to lower binding energy with the increase in the annealing temperature in Fig. 3. So, the shift toward lower binding energy for Ti 2p and O 1s positions in annealing TiO_2 NRAs can be attributed to the higher surface oxygen defect density. The relationship is also discussed in the Ref. [47]. The increase in the surface oxygen defects can trap the more photoinduced electrons, resulting in the suppression of the electron–hole recombination, which can improve charge transportation and enhance the PEC performances.

Low-resolution TEM (LR-TEM) and high-resolution TEM (HR-TEM) analysis

In order to gain more microstructure information, LR-TEM, HR-TEM and the selected area electron diffraction (SAED) analysis has been carried out to investigate the microstructures of the pristine and TiO_2 annealed at 450 °C in Fig. 4. It is noted that the TEM images of the nanorods come from the same sample before and after the annealing treatment.

In Fig. 4a, the as-prepared TiO_2 image is shown in the LR-TEM. It is found that the TiO_2 nanorod consists of multiple smaller size columns and their length and effective diameter are not uniform, which is in accordance with the clustered apexes appeared in the SEM observations [42]. Figure 4b shows the morphology of the sample annealed at 450 °C in the LR-TEM. It is found that the columns in the top of
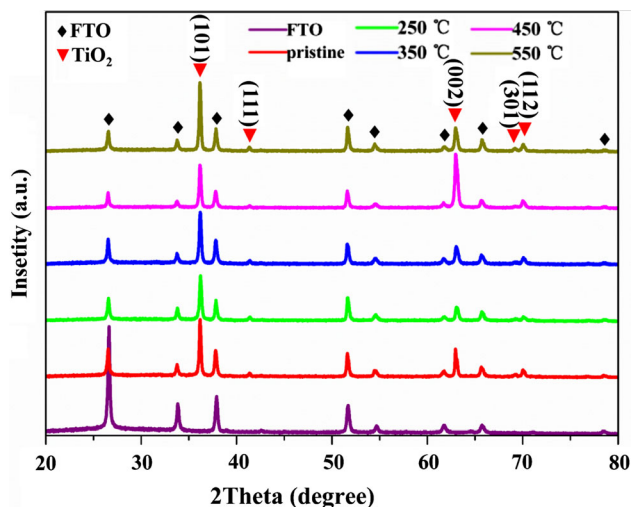
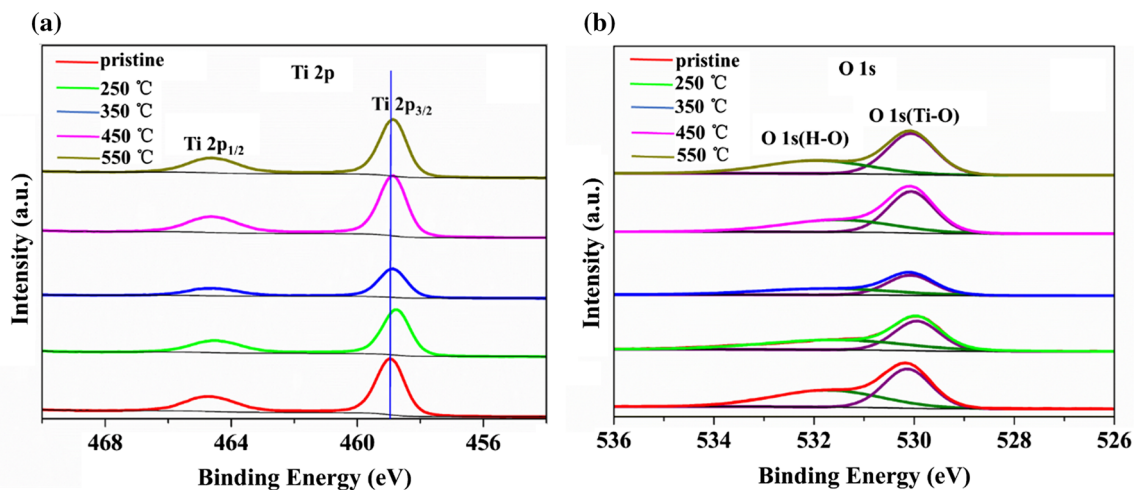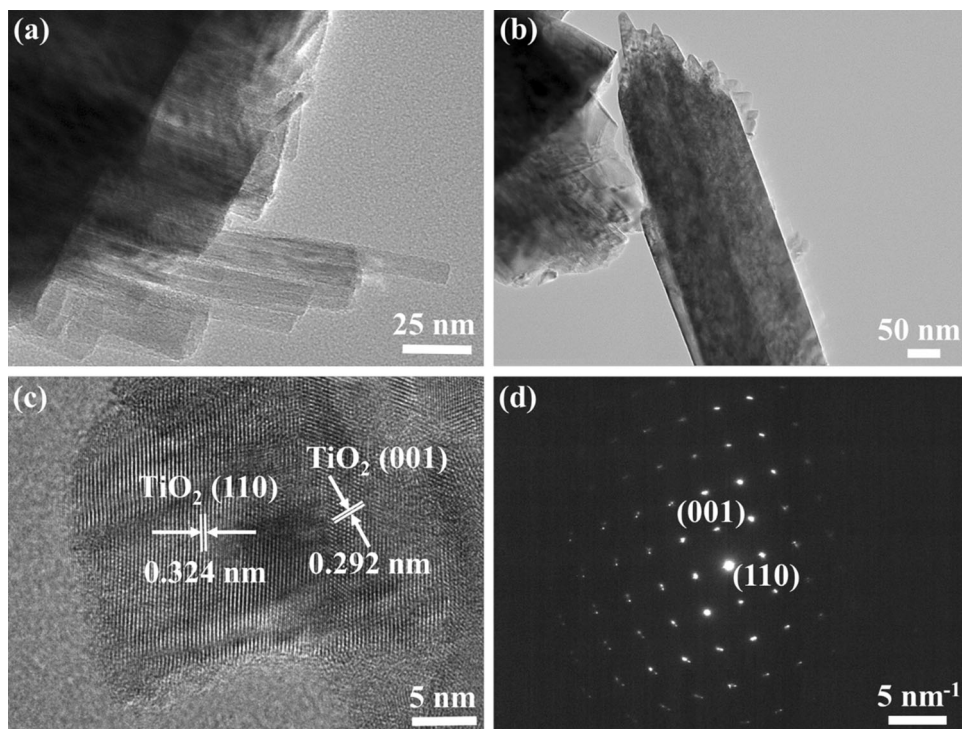**Figure 2** XRD diffraction patterns of FTO, the pristine and annealing TiO_2 NRAs.

(a)

(b)

Figure 3 XPS spectra of all the samples: **a** Ti 2p and **b** O 1s.

Figure 4 a LR-TEM image of the pristine TiO_2, **b** LR-TEM image of the TiO_2 annealed at 450 °C, **c** HR-TEM image and **d** the SAED pattern.

TiO_2 nanorod have disappeared and the top of the nanorod has become smooth and compact. As a result, the UV–Vis absorption spectrum and transport characteristics of charge carriers after annealing treatment can be improved.

The HR-TEM image and SAED pattern of the sample annealed at 450 °C are shown in Fig. 4c, d. The comparing results are shown that the differences of the HR-TEM image and SAED analysis for the annealed and the pristine samples are trivial.

As shown in Fig. 4c, the measured lattices of 0.324 nm and 0.292 nm correspond to the (110) and (001) plane of TiO_2, respectively, which are in agreement with the Refs. [35, 36, 53]. As shown in Fig. 4d, the SAED patterns exhibit the diffraction fringes composed of many separate spots, so the HR-TEM image and SAED results further confirm that the as-prepared and annealed TiO_2 NRAs are made up of single-crystalline TiO_2 columns.

UV–Vis absorption spectra

In order to evaluate the optical performance of the pristine and TiO_2 NRAs annealed at different temperatures, UV–Vis absorbance spectra carried out from 350 to 700 nm are recorded in Fig. 5. There are two aspects to explain. On the one hand, it can be found that the pristine and annealing TiO_2 NRAs show the similar absorbance spectra. However, the absorbing intensity of TiO_2 NRAs is gradually reduced from 350 to ~ 390 nm as the annealing temperature increases. Furthermore, the absorption peak frequency of all the samples appears at about 370 nm in the UV region. On the other hand, it is found that the intrinsic absorption edge of the pristine TiO_2 can be observed at ~ 410 nm. However, the absorption edge of the TiO_2 NRAs annealed at 450 °C and 550 °C can redshift to ~ 420 nm. As shown in Fig. 5, the band edges are found to be redshifted gradually as the annealing temperature increases. These results may be caused by the suppressed spacing of crystal lattice resulted from annealing process, and electrons of the different energy level become closer, which is consistent with TEM analysis.

The Tauc plots of all the samples are shown in Fig. 6. For many crystal semiconductor films, the relation between the incident photon energy hv and the absorbance coefficient α can be given by the following function [45, 54, 55]:

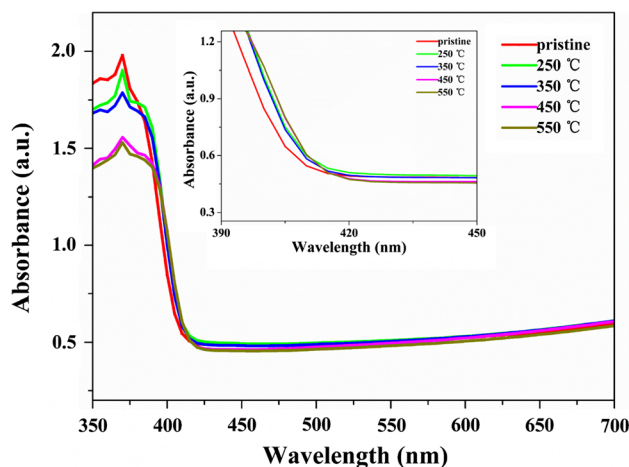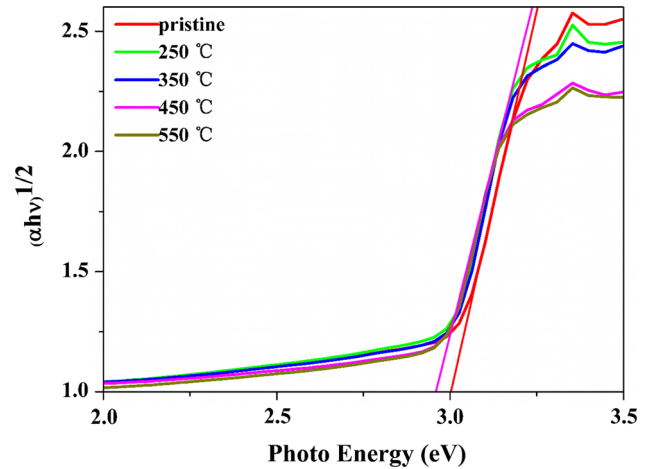$$(\alpha hv)^{1/2} = A(hv - E_g), \tag{2}$$

Figure 6 Band-gap of pristine and annealing TiO_2 NARs.

where α is the absorbance coefficient, h is Planck's constant, v is incident photon frequency, E_g is band-gap of the semiconductor material, and A is a constant. The band-gap of the pristine sample is about 3.0 eV, which is consistent with the results reported elsewhere [11]. The energy gap of the samples annealed at 450 °C and 550 °C is about 2.95 eV, which is slightly narrower than that of the non-annealing TiO_2. Although the difference between the non-annealing and annealing is not very remarkable, it is expected that the annealing treatment may improve the PEC performances.

The PEC performances

As shown in Fig. 7, the PEC performances of the pristine and annealing TiO_2 NRAs are surveyed by an electrochemical station (CHI660E, CH Instrument Inc, Shanghai) in a standard three-electrode configuration, where the illumination is 100 mW cm^{-2} with 500 W Xenon lamp in a sunlight simulator equipped with an AM 1.5G global filter. The PEC measurements are taken in the system, where the TiO_2 samples act as a working electrode, the Pt plate and Ag/AgCl (saturated KCl) as a counter electrode and a reference electrode, respectively. The electrolyte in the PEC measurement is 0.5 M Na_2SO_3 solution.

Figure 7a shows the characteristic LSV curves of the photoanode samples. The measuring voltage span is from − 0.5 to 1.0 V versus Ag/AgCl. There are three aspects to be illustrated:

First, it is found that the photocurrent intensity is improved gradually with the annealing temperature
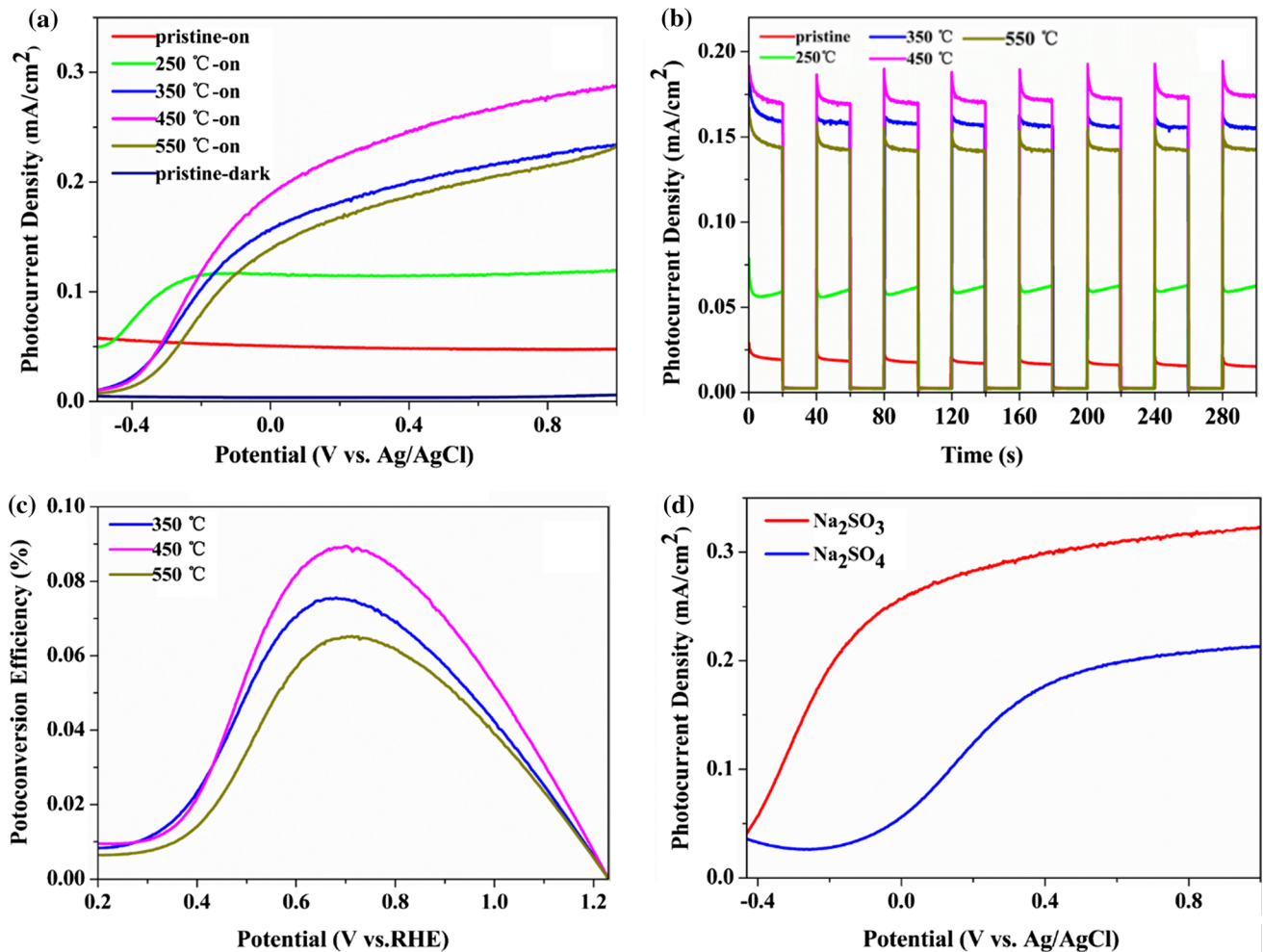
Figure 5 UV–Vis absorbance spectra of pristine and annealing TiO_2 NRAs.

Figure 7 PEC performances for the TiO$_2$ NARs: **a** J–V curves, **b** transient I–t curves, **c** the photoconversion efficiency and **d** J–V curves of TiO$_2$ annealed at 450 °C in different electrolyte.

increase. However, the decrease in photocurrent intensity is observed beyond 450 °C, which could be explained that the TiO$_2$ NARs annealed at 450 °C show the optimal PEC performance. The experiment result can be displayed that the effect of the annealing temperature for photocurrent intensity shows saturation. The photocurrent intensity of the pristine TiO$_2$ NRAs is ∼ 0.05 mA cm^{-2}, while the photocurrent intensity of the TiO$_2$ annealed at 450 °C can reach to ∼ 0.27 mA cm^{-2}. In this work, it is discovered that the optimized parameter is at 450 °C. The value of the photocurrent intensity is about six times higher than that of the original TiO$_2$ sample when its photocurrent intensity reaches saturation.

Second, the bias voltages of the saturation photocurrent intensity of the different photoanodes increase gradually with the annealing temperature increment. As we all know, crystal lattice can

produce elastic collisions for the charge carriers. The phenomenon can be explained that the charge carriers suffer from more elastic collisions due to TiO$_2$ NARs shrink. Therefore, they need higher bias voltage to overcome the more elastic collisions with the annealing temperature increment. Although the sample annealed at 550 °C enlarges the absorption spectrum in Fig. 5, the increasing elastic collisions of charge carriers will result in the decline of the drift coefficient. The two processes compete with each other, and the latter is dominant in the case, so it leads to the decrease in the photocurrent intensity with annealing temperature increment. The dark photocurrent intensity of all the samples was measured, and it is shown that the dark photocurrent intensity is almost ignored with comparing to the other photocurrent intensity under the illumination. However, the optimized annealing parameter is

beneficial to the PEC activity, otherwise the higher annealing temperature will affect the transport characteristic of charge carriers so it will deteriorate PEC performance, which is in accordance with the above characterization analysis and the previous report [47].

Third, it is found that the saturation photocurrent intensities of the pristine and TiO$_2$ NRAs annealed at 250 °C are slightly descending and that of the other three annealing photoelectrodes are slightly increasing as the applied bias is gradually improved. In other words, the phenomenon can be elucidated that the saturation photocurrent intensities of samples can be affected by the annealing temperature.

In order to evaluate the photocurrent temporal responses of all the samples, the curves of the transient photocurrent response versus time (I–t curves) are shown in Fig. 7b. The I–t curve measurements were taken in the three-electrode configuration cell under the illumination with several 40 s light on/off cycles (0.025 Hz) at 0 V versus Ag/AgCl. Based on the result, it is found that the photocurrent of all the samples is nearly zero under the dark condition, while photocurrent intensity rapidly increases to a steady-state value after the illumination, which reveals a good photoresponse behavior of all the samples. The obvious increment of photocurrent intensity under the illumination is because of the more photoinduced charge carriers in TiO$_2$ photoanodes. The result confirms that the photoelectrons are swiftly separated and transported to FTO along the TiO$_2$ nanorods in all the samples. Simultaneously, it is found that the annealing TiO$_2$ NRAs exhibit a very important effect on photocurrent density, and the TiO$_2$ NRAs annealed at 450 °C are the highest photocurrent intensity. The trend of the photocurrent response is consistent with J–V curves in Fig. 7a, indicating that the optimized annealing temperature can enlarge the absorption edge of the visible light and promote the PEC performances. The results are in accordance with the characteristic of the absorption spectra. What's more, the photocurrent densities are reproducible for several on/off cycles, which display the stability of all the samples. The annealing time influence for the PEC performance of TiO$_2$ NARs has been provided in the supplement information.

Based on Fig. 7a, the photoconversion efficiency η of the samples can be quantitatively calculated in terms of the following equation [28, 56, 57]:

$$\eta = \left[I(1.23 - V)/J_{\text{light}} \right], \tag{3}$$

where I is the photocurrent intensity (mA cm^{-2}), V is the applied bias versus RHE, and J$_{\text{light}}$ is the incident light density of 100 mW cm^{-2} (AM 1.5G). The calculated results are plotted as a function of the applied bias and the efficiency η of the samples for the annealing temperature from 350 to 550 °C are exhibited in Fig. 7c. It is found that the η of the TiO$_2$ annealed at 450 °C is ∼ 0.089% at an applied voltage of − 0.076 V versus Ag/AgCl (0.7 V vs. RHE). The low η can be due to reason of the wide band-gap, but it is the highest η comparing with the pristine TiO$_2$ NRAs. It is indicated that the annealing treatment benefits PEC activity for TiO$_2$ NRAs.

In order to evaluate the photocurrent influence of the different electrolyte, Fig. 7d shows that the LSV curves of two kinds of electrolyte are recorded in the measurement process. The photocurrent measurement is taken in a standard three-electrode configuration cell under the illumination, and the concentration of the every kind of electrolyte is 0.5 M. The measuring samples are annealed at 450 °C for 1 h. It is exhibited that the saturation photocurrent intensities of the 0.5 M Na$_2$SO$_3$ and Na$_2$SO$_4$ are about 0.31 and 0.20 mA cm^{-2}, respectively. Based on the report [36, 58], the higher photocurrent intensity in the 0.5 M Na$_2$SO$_3$ electrolyte solution comparing to another electrolyte solution is because SO$_3^{2-}$ as a scavenger consumes the holes in valance band of TiO$_2$ and reduces the recombination of electrons and holes. Therefore, it is beneficial to the efficient separation of the photoinduced charge carriers and improves the photocurrent intensity.

Photoluminescence emission spectra

In order to further comprehend the role of annealing samples in the PEC process, the PL spectra of all the samples have been carried out at room temperature, as shown in Fig. 8. It is well known that the PL spectra are an important tool to analyze the recombination rate of the electrons and holes in semiconductor materials. Its principle is that the photon-excited electrons are transferred from the valance band to the conductance band, resulting in the holes left in the valance band, where electron–hole pairs can undergo a recombination process with the photon emission [32, 37].
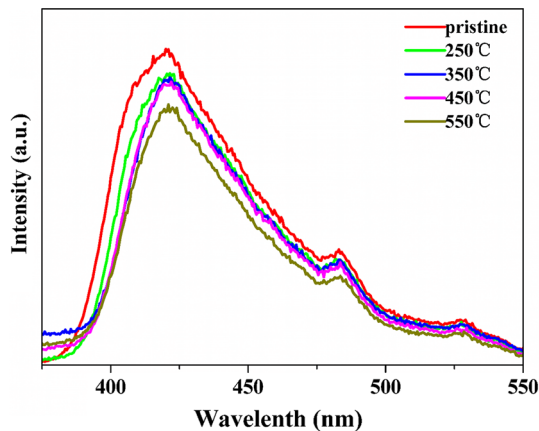
Figure 8 PL spectra of all the samples.

Therefore, the PL spectra determine the photocurrent and temporal response, etc. The lower PL intensity could explain a lower recombination rate of the photoexcited electrons and holes [34, 43]. There are main two aspects to explain for the PL spectra in the paper. On the one hand, it can find that the three main emission peaks are located in about 421, 483 and 527 nm, respectively. As shown in Fig. 8, an emission peak appears at around 421 nm, which is taken for near band edge emission (NBE) of the rutile TiO_2 crystal [43, 59]. The NBE is due to the radiative recombination of electrons from the conduction band to the valence band. Other emissions around 483 and 527 nm can be attributed to the various defects, such as oxygen vacancies, interstitial Ti and surface oxygen vacancies [34, 59]. On the other hand, it can be found that the PL spectra intensity of the pristine sample is the strongest and that of annealing samples is gradually decreasing as the annealing temperature increases except for the sample annealed at 550 °C. It can be illustrated that the recombination rate of the electrons and holes is gradually suppressed effectively due to various defects, resulting in photocurrent improvement based on above the principle in Fig. 7a. The result is consistent with the analysis of XPS spectra and the PEC performance. However, the behavior of the sample annealed at 550 °C is anomaly, which can be due to the excessive annealing temperature resulting in deteriorating the sample transmission characteristic, which leads to the decrease in the photocurrent density.

Mechanism of annealing effects on the PEC performances

It is argued that the mechanism of how annealing treatments can improve the PEC performances of TiO_2 lies in the nanorod shrinking effect and lattice reconstruction effect, based on the phenomenological findings in our experiments.

First, based on the XRD, XPS, SEM and TEM observations, one of the major phenomenological consequences of the annealing process is found to be the diameter of the nanorods will shrink, namely the nanorod shrinking effect. Such a behavior can be modeled by that the pristine TiO_2 nanorods are made up of a cluster of monocrystalline columns, the bonding energy between the interfaces of the columns can be slightly decreased through annealing process. Another possible reason is the suppression of the crystal clusters because of the interface variations [47]. Moreover, the annealing TiO_2 NARs can improve the interface adhesion between TiO_2 NRs and FTO layers [13, 42]. As a result, the contact area between the photon flux and the TiO_2 crystals will increase, and the enhancing interface adhesion benefits the charge transmission, so does the PEC current.

Second, based on the SEM, TEM, PL and UV–Vis absorption characterization results, the lattices of TiO_2 become compact, especially at the surface and the interfaces inside the clusters. As a result, on the one hand, the band-gap of the TiO_2 NRAs will decrease because the energy level of conduction and valence band can become close, so the photoinduced charge carriers in the annealed samples will increase under the illumination, which leads to the increase in the photocurrent density. On the other hand, the charge carriers in TiO_2 nanorods will suffer from more elastic collisions due to the compact lattices of TiO_2, resulting in decline of the drift coefficient, which leads to the decrease in the photocurrent density. Consequently, those two competing processes coupled together can explain the optimization phenomena as follows: In the low annealing temperature, the first process plays a leading role. However, the second behavior will become a more weighted role when the annealing temperature is beyond a criterion, i.e., an optimized annealing point, as shown in the experimental results.

Conclusion

In summary, the rutile TiO$_2$ nanorod arrays have been prepared by the hydrothermal route on conducting substrate and were treated at different annealing temperatures. The surface morphology, crystalline size, crystal structure, surface chemical states, band-gap, optical and photoelectrochemical performances of the pristine and TiO$_2$ NRAs annealed at different temperature in air are investigated. The result shows the saturation effect of PEC performance for the annealing TiO$_2$ photoanodes at different temperatures. At all the annealing temperature, the TiO$_2$ NRAs annealed at 450 °C showed the highest photocurrent intensity and photoconversion efficiency. Simultaneously, the photocurrent intensity effect of the different electrolyte solution and different annealing time for the TiO$_2$ NRAs annealed at 450 °C is also investigated. In short, we believe that this work can also provide an important source of information for further utilization and a mechanism knowledge of the annealing TiO$_2$ by the hydrothermal synthesized route in the photoelectrochemical water splitting.

Compliance with ethical standards

Conflict of interest The authors declare that they have no conflict of interest.

Electronic supplementary material: The online version of this article (https://doi.org/10.1007/s10853-020-04379-y) contains supplementary material, which is available to authorized users.

References

[1] Fujishima A, Honda K (1972) Electrochemical photolysis of water at a semiconductor electrode. Nature 238:37–38

[2] Cho IS, Logar M, Lee CH, Cai L, Prinz FB, Zheng X (2014) Rapid and controllable flame reduction of TiO$_2$ nanowires for enhanced solar water-splitting. Nano Lett 14:24–31

[3] Wolcott A, Smith WA, Kuykendall TR, Zhao Y, Zhang JZ (2009) Photoelectrochemical water splitting using dense and aligned TiO$_2$ nanorod arrays. Small 5:104–111

[4] Pengcheng W, Song X, Si S, Ke Z, Cheng L, Li W, Xiao X, Jiang C (2018) Significantly enhanced visible light response in single TiO$_2$ nanowire by nitrogen ion implantation. Nanotechnology 29:184005

[5] Han S, Ying-Chih P, Zheng L, Zhang JZ, Fang X (2015) Shell-thickness dependent electron transfer and relaxation in type-II core–shell CdS/TiO$_2$ structures with optimized photoelectrochemical performance. J Mater Chem A 3:22627–22635

[6] Lee Y-L, Chi C-F, Liau S-Y (2010) CdS/CdSe co-sensitized TiO$_2$ photoelectrode for efficient hydrogen generation in a photoelectrochemical cell. Chem Mater 22:922–927

[7] Baker DR, Kamat PV (2009) Photosensitization of TiO$_2$ nanostructures with CdS quantum dots: particulate versus tubular support architectures. Adv Funct Mater 19:805–811

[8] Karuturi SK, Shen H, Duong T, Narangari PR, Yew R, Wong-Leung J, Catchpole K, Tan HH, Jagadish C (2018) Perovskite photovoltaic integrated CdS/TiO$_2$ photoanode for unbiased photoelectrochemical hydrogen generation. ACS Appl Mater Interfaces 10:23766–23773

[9] Pawar SA, Patil DS, Lokhande AC, Gang MG, Shin JC, Patil PS, Kim JH (2016) Chemical synthesis of CdS onto TiO$_2$ nanorods for quantum dot sensitized solar cells. Opt Mater 58:46–50

[10] Shin K, Yoo J-B, Park JH (2013) Photoelectrochemical cell/dye-sensitized solar cell tandem water splitting systems with transparent and vertically aligned quantum dot sensitized TiO$_2$ nanorod arrays. J Power Sources 225:263–268

[11] Liu B, Wang D, Wang L, Sun Y, Lin Y, Zhang X, Xie T (2013) Glutathione-assisted hydrothermal synthesis of CdS-decorated TiO$_2$ nanorod arrays for quantum dot-sensitized solar cells. Electrochim Acta 113:661–667

[12] Liu B, Aydil ES (2009) Growth of oriented single-crystalline rutile tio$_2$ nanorods on transparent conducting substrates for dye-sensitized solar cells. J Am Chem Soc 131:3985–3990

[13] Gu XQ, Zhao YL, Qiang YH (2012) Influence of annealing temperature on performance of dye-sensitized TiO$_2$ nanorod solar cells. J Mater Sci: Mater Electron 23:1373–1377

[14] Xiao-Qiong W, Shao Z-D, Liu Q, Xie Z, Zhao F, Zheng Y-M (2019) Flexible and porous TiO$_2$/SiO$_2$/carbon composite electrospun nanofiber mat with enhanced interfacial charge separation for photocatalytic degradation of organic pollutants in water. J Colloid Interface Sci 553:156–166

[15] Daya Mani A, Subrahmanyam Ch (2016) One pot synthesis of CdS/TiO$_2$ hetero-nanostructures for enhanced H$_2$ production from water and removal of pollutants from aqueous streams. Mater Res Bull 73:377–384

[16] Qiu X, Burda C (2007) Chemically synthesized nitrogen-doped metal oxide nanoparticles. Chem Phys 339:1–10

[17] Yao H, Wuyou F, Yang H, Ma J, Sun M, Chen Y, Zhang W, Di W, Lv P, Li M (2014) Vertical growth of two-dimensional TiO$_2$ nanosheets array films and enhanced photoelectrochemical properties sensitized by CdS quantum dots. Electrochim Acta 125:258–265

[18] Cho IS, Choi J, Zhang K, Kim SJ, Jeong MJ, Cai L, Park T, Zheng X, Park JH (2015) Highly efficient solar water splitting from transferred TiO$_2$ nanotube arrays. Nano Lett 15:5709–5715

[19] Khan Shahed U M, Al-Shahry M, Ingler WB Jr (2002) Efficient photochemical water splitting by a chemically modified n-TiO$_2$. Science 297:2243–2245

[20] Park JH, Kim S, Bard AJ (2006) Novel carbon-doped TiO$_2$ nanotube arrays with high aspect ratios for efficient solar water splitting. Nano Lett 6:24–28

[21] Yuan J, Chen M, Shi J, Shangguan W (2006) Preparations and photocatalytic hydrogen evolution of N-doped TiO$_2$ from urea and titanium tetrachloride. Int J Hydrog Energy 31:1326–1331

[22] Asahi R, Morikawa T, Ohwaki T, Aoki K, Taga Y (2001) Visible-light photocatalysis in nitrogen-doped titanium oxides. Science 293:269–271

[23] Selvam K, Swaminathan M (2012) Nano N-TiO$_2$ mediated selective photocatalytic synthesis of quinaldines from nitrobenzenes. RSC Adv 2:2848–2855

[24] Wang W, Tadé MO, Shao Z (2018) Nitrogen-doped simple and complex oxides for photocatalysis: a review. Prog Mater Sci 92:33–63

[25] Garlisi C, Lai C-Y, George L, Chiesa M, Palmisano G (2018) Relating photoelectrochemistry and wettability of sputtered Cu- and N-Doped TiO$_2$ thin films via an integrated approach. J Phys Chem C 122:12369–12376

[26] Hong X, Wang Z, Cai W, Feng L, Zhang J, Yang Y, Ma N, Liu Y (2005) Visible-light-activated nanoparticle photocatalyst of iodine-doped titanium dioxide. Chem Mater 17:1548–1552

[27] Umebayashi T, Yamaki T, Itoh H, Asai K (2002) Band gap narrowing of titanium dioxide by sulfur doping. Appl Phys Lett 81:454–456

[28] Ming X, Da P, Haoyu W, Zhao D, Zheng G (2012) Controlled Sn-doping in TiO$_2$ nanowire photoanodes with enhanced photoelectrochemical conversion. Nano Lett 12:1503–1508

[29] Cho IS, Lee CH, Feng Y, Logar M, Rao PM, Cai L, Kim DR, Sinclair R, Zheng X (2013) Codoping titanium dioxide nanowires with tungsten and carbon for enhanced photoelectrochemical performance. Nat Commun 4:1723

[30] Bian J, Huang C, Wang L, Hung T, Daoud WA, Zhang R (2014) Carbon dot loading and TiO$_2$ nanorod length dependence of photoelectrochemical properties in carbon dot/TiO$_2$ nanorod array nanocomposites. ACS Appl Mater Interfaces 6:4883–4890

[31] Huijun Yu, Zhao Y, Chao Zhou L, Shang YP, Cao Y, Li-Zhu W, Tung C-H, Zhang T (2014) Carbon quantum dots/TiO$_2$ composites for efficient photocatalytic hydrogen evolution. J Mater Chem A 2:3344–3351

[32] Ye M, Gong J, Lai Y, Lin C, Lin Z (2012) High-efficiency photoelectrocatalytic hydrogen generation enabled by palladium quantum dots-sensitized TiO$_2$ nanotube arrays. J Am Chem Soc 134:15720–15723

[33] Sreedhar A, Jung H, Kwon JH, Yi J, Sohn Y, Gwag JS (2017) Novel composite ZnO/TiO$_2$ thin film photoanodes for enhanced visible-light-driven photoelectrochemical water splitting activity. J Electroanal Chem 804:92–98

[34] Tao J, Gong Z, Yao G, Cheng Y, Zhang M, Lv J, Shi S, He G, Jiang X, Chen X, Sun Z (2016) Enhanced optical and photocatalytic properties of Ag quantum dots-sensitized nanostructured TiO$_2$/ZnO heterojunctions. J Alloy Compd 688:605–612

[35] Liu C, Yang Y, Li J, Chen S (2018) Phase transformation synthesis of TiO$_2$/CdS heterojunction film with high visible-light photoelectrochemical activity. Nanotechnology 29:265401

[36] Zhang H, Zhang D, Qin X, Cheng C (2015) Three-dimensional CdS-sensitized sea urchin like TiO$_2$-ordered arrays as efficient photoelectrochemical anodes. J Phys Chem C 119:27875–27881

[37] Chen S, Li C, Hou Z (2019) A novel in situ synthesis of TiO$_2$/CdS heterojunction for improving photoelectrochemical water splitting. Int J Hydrog Energy 44:25473–25485

[38] Robel I, Subramanian V, Kuno M, Kamat PV (2006) Quantum dot solar cells. Harvesting light energy with CdSe nanocrystals molecularly linked to mesoscopic TiO$_2$ films. J Am Chem Soc 128:2385–2393

[39] Luo J, Ma L, He T, Ng CF, Wang S, Sun H, Fan HJ (2012) TiO$_2$/(CdS, CdSe, CdSeS) Nanorod heterostructures and photoelectrochemical properties. J Phys Chem C 116:11956–11963

[40] Mehta M, Singh AP, Kumar S, Krishnamurthy S, Wickman B, Basu S (2018) Synthesis of MoS$_2$-TiO$_2$ nanocomposite for enhanced photocatalytic and photoelectrochemical performance under visible light irradiation. Vacuum 155:675–681

[41] Fàbrega C, Andreu T, Tarancón A, Flox C, Morata A, Calvo-Barrio L, Morante JR (2013) Optimization of surface charge transfer processes on rutile TiO$_2$ nanorods photoanodes for water splitting. Int J Hydrog Energy 38:2979–2985

[42] Zhang S, Gu X, Zhao Y, Qiang Y (2016) Enhanced photoelectrochemical performance of TiO2 nanorod arrays by a 500 °C annealing in air: insights into the mechanism. J Electron Mater 45:648–653

[43] Zhao Y, Gu X, He R, Zhu L, Qiang Y (2018) Influence of annealing ambient on the photoelectric and photoelectrochemical properties of TiO$_2$ nanorod arrays. J Electron Mater 47:5251–5258

[44] Feng W, Lin L, Li H, Chi B, Jian P, Li J (2017) Hydrogenated TiO$_2$/ZnO heterojunction nanorod arrays with enhanced performance for photoelectrochemical water splitting. Int J Hydrog Energy 42:3938–3946

[45] Liu Ya, Jiang J, Quan X, Li M, Guo L (2013) Photoelectrochemical performance of CdS nanorods grafted vertically aligned TiO$_2$ nanorods. Mater Res Bull 48:4548–4554

[46] Zhu C, Li C, Zheng M, Delaunay J-J (2015) Plasma-induced oxygen vacancies in ultrathin hematite nanoflakes promoting photoelectrochemical water oxidation. ACS Appl Mater Interfaces 7:22355–22363

[47] Xie Z, Shuang S, Ma L, Zhu F, Liu X, Zhang Z (2017) Annealing effect on the photoelectrochemical and photocatalytic performance of TiO$_2$ nanorod arrays. RSC Adv 7:51382–51390

[48] Jaramillo-Quintero OA, Triana MA, Rincon ME (2017) Optimization of charge transfer and transport processes at the CdSe quantum dots/TiO$_2$ nanorod interface by TiO$_2$ interlayer passivation. J Phys D Appl Phys 50:235305

[49] Liu Y, Ren F, Shen S, Chen J, Yanming F, Cai G, Wang X, Xing Z, Liang W, Zheng X, Jiang C (2018) Vacancy-doped homojunction structural TiO$_2$ nanorod photoelectrodes with greatly enhanced photoelectrochemical activity. Int J Hydrog Energy 43:2057–2063

[50] Huang H, Hou X, Xiao J, Zhao L, Huang Q, Chen H, Li Y (2019) Effect of annealing atmosphere on the performance of TiO$_2$ nanorod arrays in photoelectrochemical water splitting. Catal Today 330:189–194

[51] Ruzybayev I, Yassitepe E, Awais Ali AS, Bhatti RM, Mohamed MI, Ismat Shah S (2015) Reactive pulsed laser deposited N-C codoped TiO$_2$ thin films. Mater Sci Semicond Process 39:371–376

[52] Saharudin KA, Sreekantan S, Lai C (2014) Fabrication and photocatalysis of nanotubular C-doped TiO$_2$ arrays: impact of annealing atmosphere on the degradation efficiency of methyl orange. Mater Sci Semicond Process 20:1–6

[53] Wang H, Bai Y, Zhang H, Zhang Z, Li J, Guo L (2010) CdS quantum dots-sensitized TiO$_2$ nanorod array on transparent conductive glass photoelectrodes. J Phys Chem C 114:16451–16455

[54] Cheng C, Wang H, Li J, Yang H, Xie A, Chen P, Li S, Huang F, Shen Y (2014) Ordered macroporous CdS-sensitized N-doped TiO$_2$ inverse opals films with enhanced photoelectrochemical performance. Electrochim Acta 146:378–385

[55] Teng W, Wang Y, Huang H, Li X, Tang Y (2017) Enhanced photoelectrochemical performance of MoS$_2$ nanobelts-loaded TiO$_2$ nanotube arrays by photo-assisted electrodeposition. Appl Surf Sci 425:507–517

[56] Sujuan H, Wang B, Zhu M, Ma Y, Lv Z, Wang H (2017) High-performance 1D type-II TiO$_2$@ZnO core-shell nanorods arrays photoanodes for photoelectrochemical solar fuel production. Appl Surf Sci 403:126–132

[57] Walter MG, Warren EL, McKone JR, Boettcher SW, Mi Q, Santori EA, Lewis NS (2010) Solar water splitting cells. Chem Rev 110:6446–6473

[58] Guo S, Zhao X, Zhang W, Wang W (2018) Optimization of electrolyte to significantly improve photoelectrochemical water splitting performance of ZnO nanowire arrays. Mater Sci Eng, B 227:129–135

[59] Soundarrajan P, Sankarasubramanian K, Sethuraman K, Ramamurthi K (2014) Controlled (110) and (101) crystallographic plane growth of single crystalline rutile TiO$_2$ nanorods by facile low cost chemical methods. CrystEngComm 16:8756–8768